International Journal of Thermal Sciences 98 (2015) 81–89

Contents lists available at ScienceDirect

International Journal of Thermal Sciences

journal homepage: www.elsevier.com/locate/ijts

Natural convection in thermal plumes emerging from a single heat source

R.H. Hernández

LEAF-NL, Departamento de Ingeniería Mecánica, Universidad de Chile, Casilla, 2777, Santiago, Chile

ARTICLE INFO

Article history:
Received 22 August 2013
Received in revised form
23 August 2014
Accepted 18 June 2015
Available online 30 July 2015

Keywords:
Natural convection
Thermal plumes
Instabilities

ABSTRACT

We report numerical simulations of confined natural convection from a single heat source, leading to the evolution of thermal plumes in two and three dimensions. Thermal plumes are driven through a single heat source mounted flush at the bottom of a slender cavity where vertical and top walls are isothermal heat sinks. Velocity and temperature fields were obtained for two Prandtl numbers, $P = 0.025, 0.71$ at three different values of the Rayleigh number, $R = 10^4, 5 \times 10^4, 10^5$ and for different box aspect ratios. Two kind of flow solutions were found: (i) Steady states corresponding to stable thermal plumes characterized by a well defined flow circulation inside the cavity and (ii) periodic states where both the flow and thermal fields oscillate in time. Unsteadiness of fluid and thermal flows is favored by choosing low Prandtl number fluids, working at high Rayleigh numbers inside high aspect ratio cavities. Instabilities are characterized by a periodic and propagative motion of the thermal plume in both transverse and vertical direction. It can be attributed to destabilizing shear stresses between ascending and descending fluid layers.

1. Introduction

Thermal plumes associated to the convective motion originated from localized heat sources, where hot fluid penetrates into a colder region above, are special cases of non linear driven flows systems where buoyancy is steadily supplied [1]. Thermal plumes created in closed environments (boxes) are very sensitive to thermal forcing and boundary conditions, specially in the case of high aspect ratio or slender cavities. Bifurcated states are readily set up accompanied by saturated oscillatory solutions with particular eigen modes (frequency and wavelength) which depend on the fluid physical properties, the amplitude of the forcing parameter and box dimensions.

From a physical viewpoint, particular emphasis on the shape and time dynamics of thermal plumes has been devoted [2] indicating that in some situations it can be considered a problem of pattern formation. The fluid near the heat source receives heat increasing its buoyancy, allowing the development of a primary fluid pattern which evolves finally to a well known thermal plume. As the plume rises losses its connection with the source which produced it [1], in particular when the plume develops inside a large container. The evolution of the cap of the plume at the first stages of its formation reveals certain non linear properties which have been explored through different numerical approaches [4,5] and observed in nice experiments [6].

Experimental and theoretical works frequently dealt with point or line heat sources [6,7] considered as a fundamental phenomena in natural convection heat transfer. Of increased complexity is the case of thermal plumes emerging from finite size heat sources [3,4] where numerical predictions can be useful in determining both the heat transfer and temporal evolution of such objects. The case of round heat sources has been recently considered as a basic setup for the determination of instability modes in a mechanically driven thermal plume by ultrasound scattering [8]. Scattering of sound waves of high frequency can be used a powerful non-disturbing tool to measure experimentally all spatial length scales of an unstable thermal plume [9].

Another important view point is the role of small-scale plumes emerging from discrete heat sources in 3D hard Rayleigh–Bénard turbulence. For instance, the abrupt detachment of very small hot regions (plumes) from a wall could be the physical mechanism responsible for the different scalings laws when soft and hard turbulence are considered [10]. Examples of confined natural convection flows from finite size heat sources have been reported long time ago [11] as an effort to understand the efficiency of discrete

E-mail address: rohernan@ing.uchile.cl.

http://dx.doi.org/10.1016/j.ijthermalsci.2015.06.010
1290-0729/

Nomenclature

g	gravitational acceleration
W, H	box dimensions in x, y coordinates respectively
Nu	local Nusselt number $u_i\theta - \frac{\partial\theta}{\partial x_i}$ in direction i
$\langle Nu\rangle_x(t)$	wall averaged Nusselt number
p	dimensionless pressure
P	Prandtl number ν/α
R	Rayleigh number $g\beta\Delta TW^3/\nu\alpha$
t, f_0	dimensionless time and frequency respectively
T_h, T_0	hot and cold temperatures respectively
u, v	dimensionless x, y components of velocity respectively
x, y	dimensionless coordinates
α	thermal diffusivity
β	coefficient of thermal expansion
δt	discrete time step
ΔT	temperature difference $(T_h - T_0)$
$\delta x, \delta y$	discrete steps in x, y coordinates respectively
$\delta\theta$	contour intervals for isotherms
Γ_{xy}	aspect ratio $H/W = 5$
λ	dimensionless wavelength
ν	kinematic viscosity
Θ	dimensionless temperature $(T - T_0)/(T_h - T_0)$
ρ	fluid density
τ_d	diffusive time scale W^2/α

heaters in particular configurations as passive elements in electronic cooling [3,12].

The scope of this work is to examine the heat transfer and natural convection of two-dimensional thermal plumes emerging from a small heat source mounted flush with the bottom of a slender cavity in a thermally uniform environment. Using a numerical approach we will solve the governing equations and provide accurate results for the local and overall dynamics of thermal plumes in the case of two different Prandtl numbers ($P = 0.025, 0.71$) at different values of the governing parameter, the Rayleigh number R and for different cavity's aspect ratio. The onset of time dependent solutions will be validated by comparison with three-dimensional numerical simulations of similar situations. These results will be provided just to confirm the range of validity of the two-dimensional approximation, which indeed will represent much lower computational costs.

2. Formulation

The physical situation (see Fig. 1) corresponds to a small heat source of length b located at the bottom (center) of a slender cavity of aspect ratio $H/W = 5$. The heat source of size b ($W = 10b$) has a uniform and constant temperature T_h, while the side walls and the top wall are kept at uniform temperature T_0 ($T_h > T_0$). The rest of the bottom wall is thermally insulated. Velocity vanishes on rigid walls. The 2D Boussinesq governing equations, retaining time derivatives in dimensionless form are the mass, momentum and energy conservation equations,

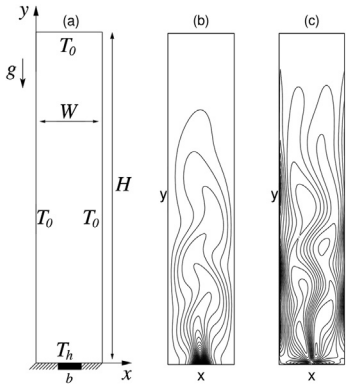

Fig. 1. (a) Schematic of the physical set up. A slender 2D cavity of aspect ratio $\Gamma_{xy} = H/W = 5$ with a localized heat source of size b ($W/b = 10$) at constant temperature T_h, at the bottom wall center. The rest of the bottom wall is adiabatic and lateral and top walls have temperature $T_0 < T_h$. Gravity vector is $\mathbf{g} = -g\hat{y}$. (b) A typical instability is represented by temperature iso-contours (iso-contour interval is $\delta\theta = 0.02$) at $R = 10^5$ and $P = 0.71$. (c) Iso-contours of vorticity (Ω) showing the periodic structure of the unstable thermal plume at $R = 10^5$ and $P = 0.71$ (iso-contour interval is $\delta\Omega = 1.6$).

$$\nabla\cdot\mathbf{u} \tag{1}$$

$$\frac{\partial\mathbf{u}}{\partial t} + \mathbf{u}\cdot\nabla\mathbf{u} = -\nabla p + R\,P\,\theta + P\nabla^2\mathbf{u}; \tag{2}$$

$$\frac{\partial\theta}{\partial t} + \mathbf{u}\cdot\nabla\theta = \nabla^2\,\theta \tag{3}$$

The governing parameter is the Rayleigh number $R_y = g\beta\Delta TL^3/\nu\alpha$ ($R_x = 0$), where the choice for the characteristic length scale L has been the distance between the hot and cold walls, i.e., $L = W$ as the shortest characteristic distance between the heat source and cold lateral walls. The fluid Prandtl number is the ratio between the conduction and viscous times scales, $P = \nu/\alpha$, where α is the thermal diffusivity and ν the kinematic viscosity. The temperature difference between the heat source and the environment is $\Delta T = T_h - T_0$, g is the gravitational acceleration and β the thermal expansion coefficient.

Non dimensional equations were obtained by means of the following scaling; time, velocity and pressure were scaled using $W^2/\alpha, \alpha/W, \rho(\alpha/W)^2$ respectively as reference quantities, where ρ is the fluid density. Coordinates were scaled with the horizontal dimension of the cavity W and the dimensionless temperature was defined as $\theta = (T - T_0)/(T_h - T_0)$.

In the context of our problem variables, the boundary conditions are the following: Fluid velocity vanishes on rigid walls and temperature T_h is imposed at the locally heated portion of the bottom wall, b. Temperature of vertical and top walls is T_0. In dimensionless form we have:

$(W-b)/2 \le x \le (W+b)/2$	$y = 0$	$u, v = 0\ \theta = 1$
$0 \le x \le (W-b)/2$	$y = 0$	$u, v = 0\ \partial_y\theta = 0$
$(W+b)/2 \le x \le W)$	$y = 0$	$u, v = 0\ \partial_y\theta = 0$
$0 \le x \le W$	$y = 0$	$u, v = 0\ \theta = 0$
$x = 0, W$	$0 \le y \le H$	$u, v = 0\ \theta = 0$

Overall heat transfer quantities, like the Nusselt number, were spatially averaged over each cavity wall. By definition, the averaged Nusselt over each cavity wall is

$$\langle Nu\rangle_x(t) = \frac{1}{H}\int\left(u\theta - \frac{\partial\theta}{\partial x}\right)dy \tag{4}$$

$$\langle Nu\rangle_y(t) = \frac{1}{W}\int\left(v\theta - \frac{\partial\theta}{\partial y}\right)dx \tag{5}$$

where $\langle Nu\rangle_x(t)$ is calculated for both left and right walls and $\langle Nu\rangle_y(t)$ is calculated at the top wall.

3. Numerical procedure

These governing equations were solved in primitive variables using a finite volume formulation and the SIMPLER algorithm [13], which has been extensively used in box confined natural convection flows, performing well with Newtonian fluids in 3D situations [5,14,15] and, very recently, with non Newtonian fluids [16]. In order to confirm the consistency and accuracy of our computer code, it was validated against the benchmark results of de Vahl Davis [17]. In the present case, the discretization of the physical domain was done with a two-dimensional uniform and staggered grid of (61×301) points in the horizontal (x) and vertical (y) coordinates respectively, providing an aspect ratio $\Gamma_{xy} = 5$. As a check of grid independence, the numerical simulation was carried out on coarser and finer meshes up to (81×401) grid points. These preliminary tests with different grids allow an appropriate choice of the mesh size without compromising accuracy and CPU time. Staggered uniform grids were used with a uniform step $\delta x_i = 0.016$ giving reasonable grid independent solutions and spatial resolution as it is shown in Table 1. A time step $\delta t = 0.001$ was used in all calculations representing 0.1% of the smallest diffusive time scale $\tau_d = W^2/\alpha$. Therefore it can be considered as a small fraction of the characteristic time scales of the thermal phenomenon and at the same time should allow to resolve the smallest time scales associated to any developing instability in a convection-dominated regime.

With these definitions, an overall check of consistency of the numerical code was made in order to evaluate the residue of heat flows across the cavity. An overall residue less than 1% was considered as a good energy balance and it was incorporated as a critical condition to progress in time with our numerical code. In general, to obtain converged solutions at each time step we used a simple but accurate criteria for each of the several variables of our problem. We considered converged solutions if and only if the condition $\left|\varepsilon_{ij}^{k} - \varepsilon_{ij}^{k-1}\right| < 10^{-6}$ is satisfied by any variable ε_{ij} at each grid point (i,j), where k represents a given iteration of our code. Such a condition is very time consuming, however it is a consistent criteria for all cases here considered, specially when the system becomes unstable.

4. Results

We have focused our attention on two different Prandtl numbers; $P = 0.71, 0.025$, and for each one we solved our set of equations at three Rayleigh numbers; $R = 10^4, 5\cdot10^4, 10^5$. Steady states were only reached at moderate Rayleigh numbers $R = 10^4, 3\cdot10^4$ for $P = 0.71$ and in general, can be characterized by a thermal plume formed by a central upward flow accompanied by two symmetrical fluid loops of cold fluid moving along the lateral walls that ultimately feed the plume entrainment region close to the heat source.

A thermal plume developed inside a closed box has a very different behavior from those generated in open environments. In a closed environment, the imposed shear and thermal losses (by virtue of boundary conditions) will considerably attenuate the plume dynamics and therefore reduce the number of degrees of freedom of the system. Moreover, in a closed domain the mass conservation constraint will force the fluid to circulate along some particular paths, generating an effective or time-averaged fluid circulation pattern. In any of the tested cases, there are two closed fluid loops in the proximity of the heat source, that feed with cold fluid the lower zone of the plume. Fig. 1 shows the isotherms (b) and iso-vorticity (c) contours for a thermal plume in air $P = 0.71$ at $R = 10^5$ where the thermal field appears disturbed across the cavity as a result of the developing instability. The periodic motion originated by the instability is detected in the heat fluxes across the lateral walls, an effect which can be used to distinguish between stable and unstable states in an experimental set up.

Fig. 2(a) displays the isotherms for $P = 0.71$ at three increasing values of the Rayleigh number. Steady states found at the lowest R value are charecterized by a static plume development, where the plume penetration or plume height increases considerably with R. At $R = 10^4$ the wall-averaged Nusselt number reach a constant value and the respective plume height is rather small. For the next curve, at $R = 5\cdot10^4$, wall-averaged Nusselt number, $\langle Nu\rangle_x(t)$, displays a very small oscillation (see Table 1) attributed to the starting

Table 1
Grid independence study for aspect ratio $\Gamma_{xy} = 5$, $R = 10^4$ and $P = 0.71$.

Grid size	$\langle Nu_l\rangle_x$	$\langle Nu_r\rangle_x$	$\langle\theta\rangle$
21×101	0.1575	0.0125	0.0086
41×201	0.1061	0.1061	0.0304
61×301	0.1048	0.1048	0.0301
81×401	0.1047	0.1047	0.0301

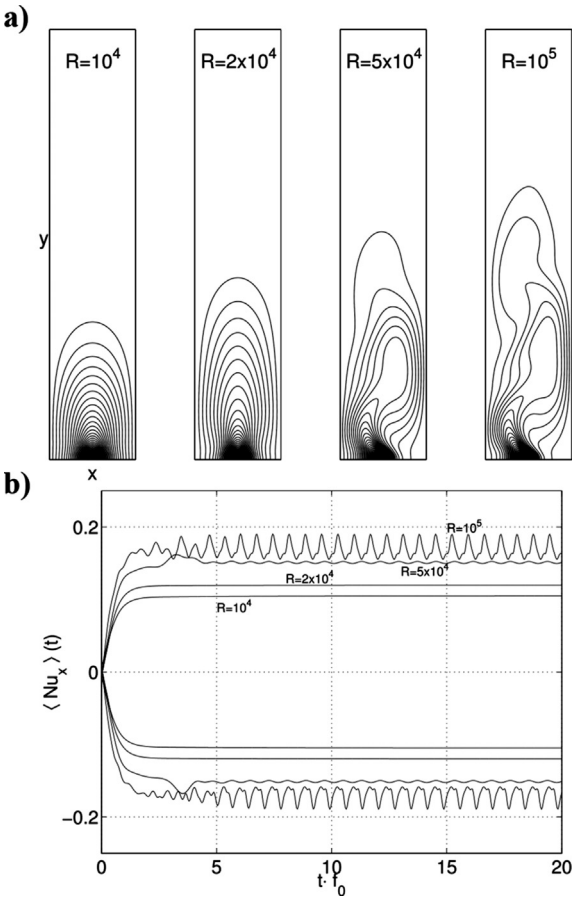

Fig. 2. Converged solutions of the thermal plume for $P = 0.71$ at $R = 10^4, 5\cdot10^4, 10^5$. (a) Iso-contours of temperature ($\delta\theta = 0.02$) (b) Temporal behavior of averaged Nusselt number, $\langle Nu\rangle_x(t)$, at side walls versus the number of cycles ($t\cdot f_0$), where t is the time and f_0 is the oscillation frequency of the instability.

instability of the thermal plume. Such a small fluctuation can not be directly observed in the respective iso-contours of temperature. On the last curve, at $R = 10^5$, the unstable plume is easily observed through a periodic thermal pattern on the cavity accompanied by the respective wall-averaged Nusselt number shown in Fig. 2(b). A clear increase of Nusselt number with Rayleigh number is observed and the unstable plume is responsible of a periodic oscillation of the local, as well as, the wall-averaged heat fluxes at the lateral walls. In all cases we get a constant time lag of half a period between maximum values of Nusselt number at opposite walls, after the long transient part. The developing instability of the third thermal plume can be characterized in the frame of a linear stability analysis by a complex growth rate σ. For short times after instability onset, linear theory predicts that instability will occur when the most unstable mode, $\sigma = \sigma_r + j\omega$, crosses the imaginary axis ($j\omega$), i.e., when $\sigma_r > 0$. If the associated frequency ω is not zero, the transition therefore corresponds to a Hopf bifurcation [18]. In our case it seems that the instability appears when we increase the Rayleigh number beyond a certain critical threshold, say R_c, but this value seems to depend on the choice of the fluid Prandtl number. After instability onset, the plume displays a spatial periodic pattern and a characteristic frequency which can be regarded as a Hopf bifurcation marking the transition between a steady and spatio-temporal periodic flow. In any case, an accurate determination of the intrinsic properties of this bifurcation is beyond the scope of this work.

A cycle of oscillation is shown in Fig. 3 for the unstable thermal plume obtained with $P = 0.71$ at $R = 10^5$. Snapshots of the isotherms were taken at times indicated by the dots in the inset of Fig. 3(b). Right wall-averaged Nusselt number $\langle Nu\rangle_x(t)$ (shown in the inset) oscillates around a mean (or dc) value where the frequency of these fluctuations is associated to the lateral periodic motion of the unstable plume. Inside the cavity, temperature fluctuations as well as velocity fluctuations have the same frequency of oscillation found in the wall-averaged Nusselt number. An important contribution to wall-averaged Nusselt number comes from the base of the plume, where high transverse velocity occur giving therefore high values of local Nusselt number that are enhanced when the starting plume bends toward the corresponding wall.

When we consider the case of small Prandtl number $P = 0.025$ we found an unstable thermal plume at any of the three Rayleigh numbers. As the initial conditions are exactly the same used in the previous runs (fluid at rest), we understand that the threshold value of Rayleigh number, R_c, not only depends on Prandtl number, but it is smaller for $P = 0.025$. Fig. 4 displays instantaneous snapshots of the isotherms at $R = 10^4, 5\cdot10^4, 10^5$ with the corresponding wall-averaged Nusselt numbers. As the Prandtl number is small, the fluid ability for momentum spreading is weaker than in the previous case, generating thermal plumes of smaller size or small penetration depth. The global dynamics is therefore concentrated at the base of the cavity as shown in Fig. 4(a). The wall-averaged Nusselt number of Fig. 4(b) displays strong periodic oscillations at each Rayleigh number R, where the relative saturated amplitude increases with R and the peak-to-peak amplitudes are important when compared to the mean Nusselt number (time averaged).

The period of oscillation here is considerably greater than that of the case $P = 0.71$ by a factor of 6 (see Table 2). In both cases the period of oscillation decreases with the Rayleigh number, meaning that the characteristic frequency of the unstable eigenmode increases with the governing parameter, and that implies that the heat flow changes its sign at increased frequencies with higher R. Another important fact is that the peak-to-peak Nusselt fluctuations are really important ($P = 0.025$) when compared to the wall-averaged Nusselt number, and they are increasing functions of the Rayleigh number as shown in the Table 1.

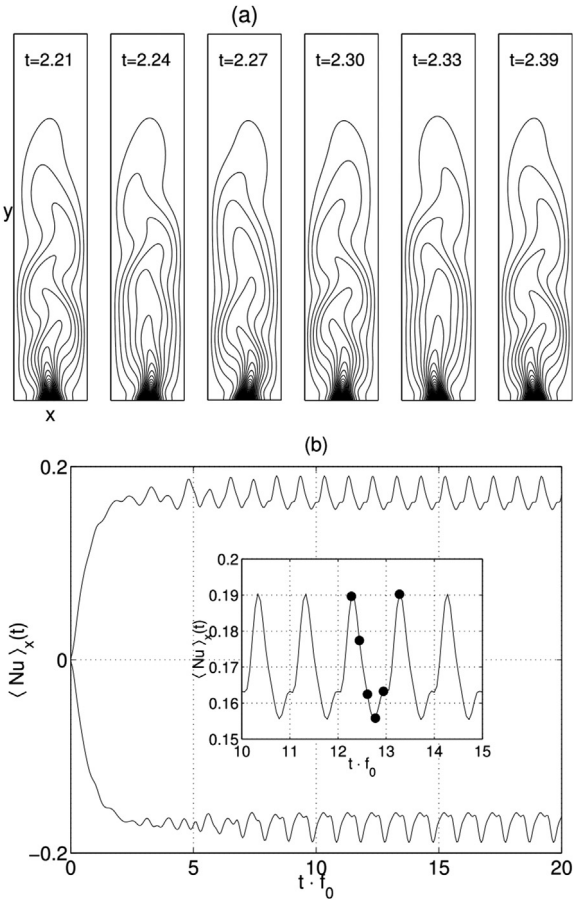

Fig. 3. (a) Snapshots of the periodic evolution of the iso-contours of the temperature field $\theta(x,y,t)$ at different times for $R = 10^5$ and $P = 0.71$ ($\delta\theta = 0.02$). (b) Associated periodic evolution of the averaged Nusselt number $\langle Nu\rangle_x$ at the left (upper curve) and right (lower curve) walls as a function of the number of cycles, given by $(t\cdot f_0)$, where t and f_0 are the time and characteristic frequency respectively. The inset indicates specific times where the snapshots were taken.

Fig. 4(b) indicates that the overall effect of increasing Rayleigh number is more important on Nusselt fluctuations rather than on the time averaged Nusselt number. If the Nusselt signal is decomposed into a dc (or time-averaged value) plus a periodic fluctuation, we see that the dc component increases only slightly with Rayleigh number. This effect means that at low Prandtl numbers heat flow across lateral walls is concentrated at the base of the cavity as the thermal plume height is small and it does not exhibit a notorious increase of plume height with R for $P = 0.025$ (see Fig. 4). On the contrary, for $P = 0.71$ the dc Nusselt value increases rapidly with R because of the notorious increase of thermal plume height with R, as shown in Fig. 3(a). The overall behavior of heat flow can be, as we said before, decomposed into a time-averaged part (dc part) due to the time-averaged plume penetration or plume height plus an oscillating part associated to the wavy behavior of the thermal plume being responsible of lateral heat flow fluctuations. As the plume height at low P is not greatly affected by R, the global dynamics become localized, giving a nearly constant dc heat flow across lateral walls. In that case, an increase in the Rayleigh number will feed with energy almost exclusively the fluctuating part.

Fig. 5 shows snapshots of isotherms for $P = 0.025$ at $R = 10^5$ accompanied with the time evolution of the wall-averaged Nusselt number. Snapshots were taken over a period of oscillation of the

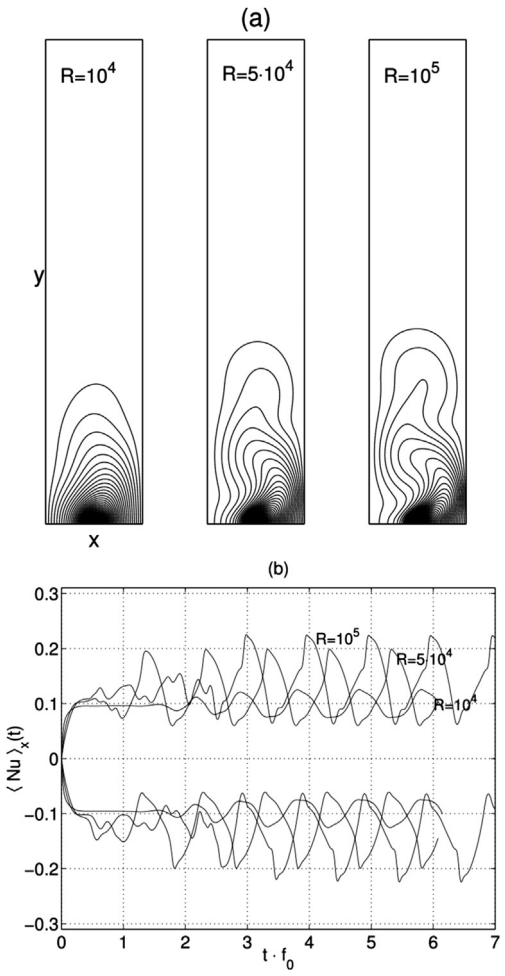

Fig. 4. Converged solutions of a thermal plume for $P = 0.025$ at $R = 10^4, 5\,10^4, 10^5$. (a) Iso-contours of temperature ($\delta\theta = 0.02$) (b) Behavior of averaged Nusselt number, $\langle Nu\rangle_x(t)$, at side walls as function of cycles of oscillation ($t \cdot f_0$).

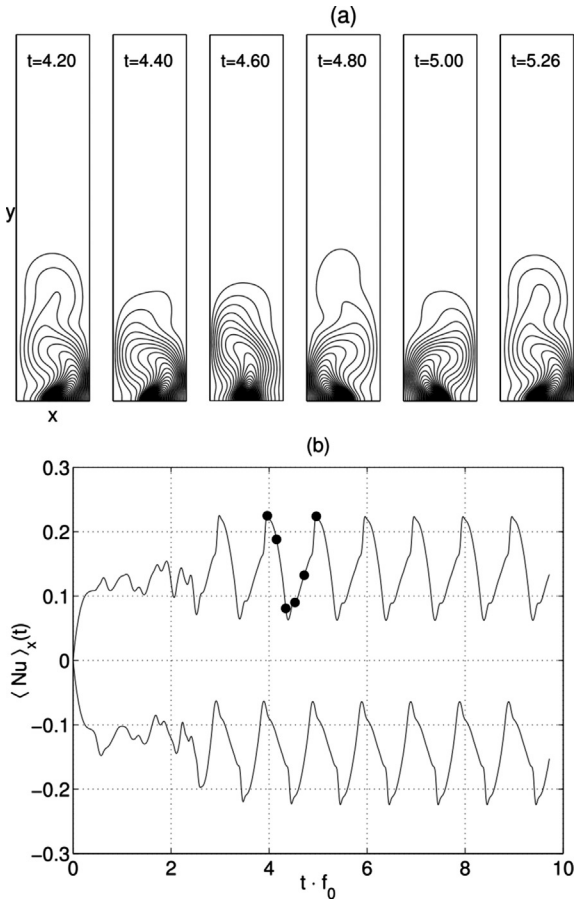

Fig. 5. (a) Snapshots of the periodic evolution of the iso-contours of the temperature field ($\delta\theta = 0.02$) at different times for $R = 10^5$ and $P = 0.025$. (b) Associated periodic evolution of the averaged Nusselt number $\langle Nu\rangle_x$ at the left (upper curve) and right (lower curve) walls as a function of the number of cycles. The dots indicates specific times where the snapshots were taken.

Nusselt number (shown by the filled dots). As in the case of $P = 0.71$ the plume oscillation is responsible of the periodic lateral heat flow fluctuations. However the plume height is about a third of the cavity height, concentrating the overall dynamics close to the heat source.

To be accurate, even here, the plume height changes periodically in time but these fluctuations are very small when compared with the size of the box. An interesting estimation of plume penetration is presented in Fig. 6. In order track in time the plume penetration depth, we record the instantaneous position of maxima of vertical fluid velocity, denoted by $x_m(t), y_m(t)$, as a function of time. In Fig. 6 we plot the time evolution of the axial and lateral position of these maxima versus time. Both are periodic functions of time, with the same frequency, showing that plume penetration, given roughly by $y_m(t)$, evolves in the form of spikes of short duration compared with the smooth behavior of the transverse position $x_m(t)$.

To get a two dimensional image of the periodic process, we built the spatial locus of the maximum velocity which can then be plotted in two dimensions across the cavity, as shown in Fig. 6(b,c,d). All spatial locus are symmetric with respect to the cavity vertical axis. There are four characteristic branches on each locus ($P = 0.025$) at each Rayleigh number. The two lateral branches indicate the transverse motion of the thermal plume approaching the lateral walls, and two nearly vertical branches at the center of the cavity indicating vertical motion of the plume. The two central branches become joined together when the Rayleigh number is increased and represent a good estimation of the intensity of the dynamical penetration depth inside the cavity.

To understand the locus timing, we see in Fig. 7(a) that between peak-to-peak horizontal cycles of $x_m(t)$, two vertical spikes of $y_m(t)$ take place. We denoted by consecutive numbers the temporal sequence on the $x_m(t)$ and $y_m(t)$ plots, that can be identified with each of the four branches of Fig. 7(b). Starting with a left branch (1), the plume rapidly raises through the cavity reaching point (2) after that the plume falls abruptly, passing by the cavity center to reach point (3) which is a lateral maximum of $x_m(t)$. The cycle is then completed when the plume raises again reaching point (4), to

Table 2
Time period (f_0^{-1}) of wall-averaged Nusselt fluctuations at right wall. We show peak-to-peak Nusselt fluctuations $\langle Nu\rangle_{pp}$ (between brackets) and the time-average of the wall-averaged Nusselt number $\overline{\langle Nu\rangle}$, at different Rayleigh numbers, R, and Prandtl numbers P.

	f_0^{-1} (period)		$[\langle Nu\rangle_{pp}]\ \overline{\langle Nu\rangle}$	
R	$P = 0.025$	$P = 0.71$	$P = 0.025$	$P = 0.71$
10^4	3.26	∞	[0.050] 0.100	[0] 0.104
$5\cdot10^4$	1.53	0.25	[0.139] 0.124	[0.002] 0.143
10^5	1.06	0.18	[0.163] 0.143	[0.035] 0.169

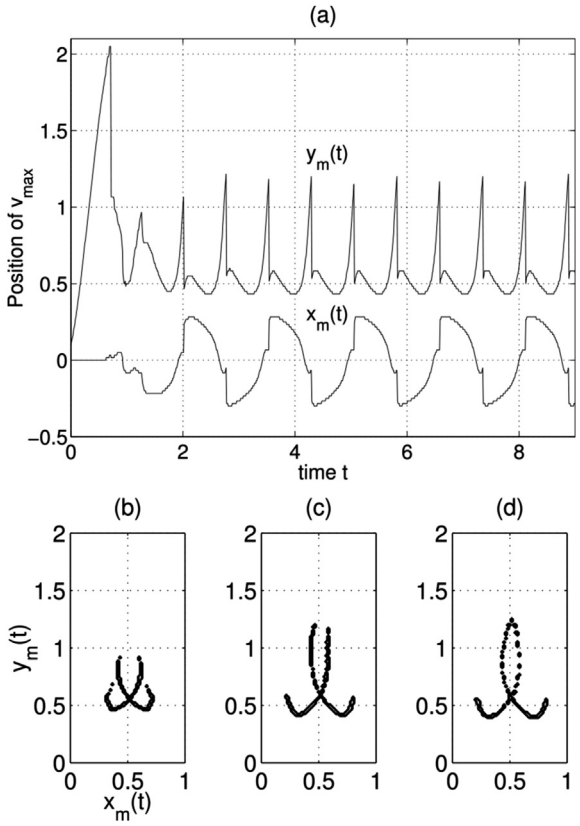

Fig. 6. (a) Evolution of plume penetration depth at $R = 5 \cdot 10^4, P = 0.025$. The plume oscillation can be observed finding the local position (x_m, y_m) of maximum v velocity versus time. After a long transient, both quantities, x_m, y_m oscillate periodically. Locus of plume penetration depth for $P = 0.025$ at (b) $R = 10^4$, (c) $5 \cdot 10^4$ and (d) 10^5. We show only the base of the cavity.

restart the cycle. The plume therefore reaches maxima of height slightly off the symmetry axis of the cavity, moving close to a lateral wall. There the spike effect of the plume is understood if we think that a plume raising near a lateral wall will increase the heat flow locally, and therefore will be cooled rapidly decreasing local buoyancy and falling again toward the heat source to restart the cycle.

The plume spatial locus is useful to understand the observed Nusselt curves of Fig. 4. The transit between lateral maxima shown in Fig. 7 is responsible of the strong Nusselt fluctuations of Fig. 4. If we consider the case $P = 0.025$ at $R = 5 \cdot 10^4$, the period of the wall-averaged Nusselt number on a wall is close to 1.5 (see Table 1), which corresponds to the period of the function $x_m(t)$ on Fig. 7. Now, the time between two consecutive peaks values at left and right walls is exactly one half, i.e. ~ 0.75 and corresponds to the same time scale between two consecutive spikes of function $y_m(t)$ (Fig. 6). Moreover, the small change in the average vertical amplitude of the locus, when we increase Rayleigh number, is responsible of the slightly different (increasing) average values of Nusselt number (see Table 1).

In the case of $P = 0.71$ the spatial locus is a vertical line at the centerline of the cavity (not shown) for the lowest Rayleigh number $R = 10^4$, because thermal plume fluctuations are very small (rather in steady state) and their highest vertical flow velocities are found at the vertical axis of the box. However if the Rayleigh number is high, as in the case of $R = 10^5$, the wall-averaged Nusselt number fluctuations are important (see for instance Fig. 3), and the spatial locus displays transverse fluctuations of similar shape as in Fig. 6 but of very small amplitude.

Even if the locus evolution is at the origin of the Nusselt fluctuations and provides a simple but clear view of the spatio-temporal character of the unstable thermal plume, the physical mechanism which drives the flow instability is not clear. A possible mechanism of flow instability, in such a slender cavity, could be attributed in part to the shear stresses between ascending and descending fluid layers, like a Kelvin–Helmholtz instability [18].

4.1. Unsteadiness and aspect ratio Γ_{xy}

The choice of a tall cavity obeys the fact that we were looking for an unsteady convection regime. Early runs with different aspect ratios have shown that such unsteadiness of the thermal and velocity fields can be triggered for high cavity aspect ratios $\Gamma_{xy} = H/W$ for a given Prandtl and Rayleigh number. For air at $R = 5 \cdot 10^4$ flow field unsteadiness starts to be seen at low aspect ratios, then it becomes the dominant flow regime inside the entire cavity.

Unsteadiness is the result of a spatio-temporal instability, and we believe that the mechanism driving the instability rely on the shear stresses between central ascending plume and the lateral descending fluid layers. In order to develop the instability, the size

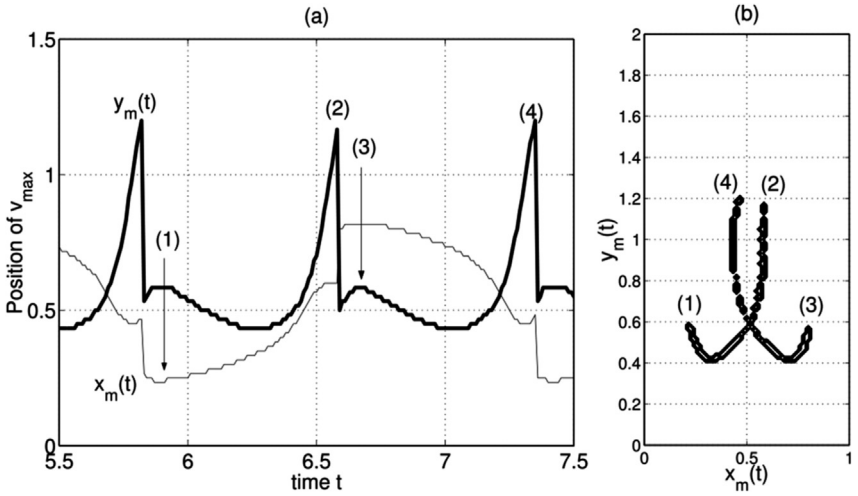

Fig. 7. (a) Details of the periodic evolution of $x_m(t)$ and $y_m(t)$ at $R = 5 \cdot 10^4$ and $P = 0.025$. (b) Locus of plume penetration depth for $P = 0.025$ at $R = 5 \cdot 10^4$. The periodic evolution is indicated on each figure by consecutive numbers, to determine the spatial sequence of the locus performed by the plume.

of the system must have enough room to fit at least one instability wavelength λ, otherwise the spatial eigenmode can not be set and the flow becomes stable. In Fig. 8 we show the same fixed number of the thermal contours as a function of the cavity aspect ratio, and we clearly see that the spatial wavelength fit the cavity size when the aspect ratio is close to $\Gamma_{xy} = 1.9$. After that, the plume feels free to oscillate and eventually propagates upwards, reaching higher but limited portions of the cavity as displayed in the locus of Fig. 7.

However, as the aspect ratio increases, the averaged heat transfer across top wall shows a marked decrease due to the thermal plume cap at a given Rayleigh number is unable to reach the top part of the cavity producing a localized thermal dynamics spatially limited to the lower part of the cavity.

In Fig. 9 we show the averaged Nusselt number as a function of the aspect ratio. It is observed that the heat transfer across the top wall is strongly dependent on Γ_{xy} becoming nearly zero when aspect ratio $\Gamma_{xy} = 5$. On the other hand, the lateral heat flux slowly decreases with Γ_{xy}, which is explained by the spatial localization of the flow and thermal dynamics on the first lower portion of the cavity. This can be observed in Fig. 8, where thermal contours starting at $\Gamma_{xy} = 3$ are very similar, i.e., they have the same spatial distribution at similar times. With no doubt, this means that further increase of the height of the cavity will have a very slight influence on the overall flow structure. Note that the transition from steady to unsteady flow occurs at $\Gamma_{xy} \sim 1.9$, exactly when the top and lateral averaged Nusselt curves of Fig. 9 intersect, and just after that the flow unsteadiness set forth as a result of the instability.

4.2. Tridimensional effects

Unsteadiness of the velocity and thermal fields in the 2D cavity represent the onset of a transverse oscillating mode of the plume. This mode may lead to the onset of longitudinal oscillation modes of the plume that may not be clearly indentified in a 2D computation. In order to check the validity and limits of the 2D approximation we have performed a full 3D numerical simulation of one

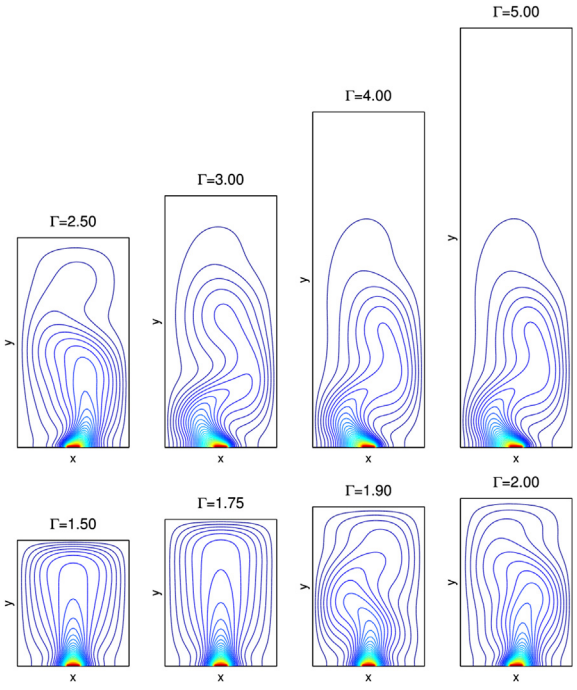

Fig. 8. Unsteadyness of field variables as a consequence of the cavity aspect ratio $\Gamma_{xy} = H/W$ at $R = 5{\cdot}10^4$ and $P = 0.71$.

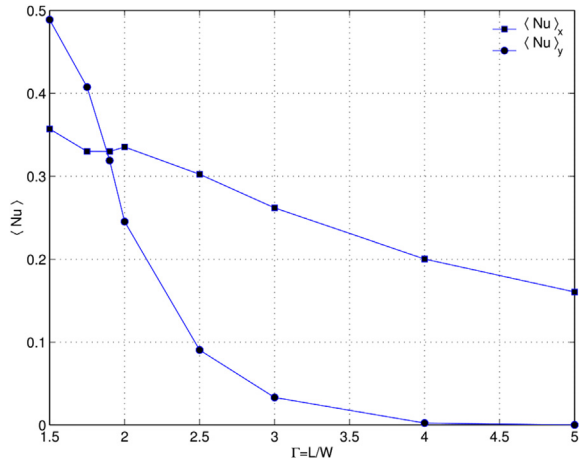

Fig. 9. Averaged Nusselt number on lateral and top wall versus cavity aspect ratio Γ_{xy} at $R = 5{\cdot}10^4$ and $P = 0.71$.

unsteady situation, with Rayleigh and Prandtl numbers $R = 10^5$ and $P = 0.71$ respectively. We considered a three dimensional (x, y, z) cartesian staggered grid of $(41 \times 201 \times 401)$ points in each coordinate respectively. By adjusting the spatial steps we define a computational domain corresponding to a cavity of same width W and height H but having a third z dimension or depth D, giving the following aspect ratios $\Gamma_{xy} = H/W = 5$ and $\Gamma_{xz} = D/W = 10$. This large aspect ratio provides enough room to develop a large portion of the thermal plume far from the wall influence by confining temperature and velocity gradients at the front $(z = 0)$ and back $(z = 10)$ walls, leaving a central cavity section where the plume complies with the two dimensional approximation, at least, in a steady state regime. The cavity has the same boundary conditions of the 2D case, i.e., no slip velocity conditions and constant temperature, T_c, on vertical and top walls. The heat source is here a heated stripe of size b mounted flush on the bottom wall that it was kept at constant temperature T_h. Discretization of the 3D domain was done with uniform steps $\delta x = \delta y = \delta z = 0.025$, with a time step of $\delta t = 10^{-3}$. In Table 3 we compare averaged heat transfer results at lateral vertical walls from both the 2D and 3D calculation.

At Rayleigh number $R = 10^4$ and Prandtl $P = 0.71$ the thermal plume developed in the 3D cavity reached a uniform and steady state thermal plume similar to the snapshots of the 2D plume of Fig. 2. At $R = 10^5$ and $P = 0.71$ the situation is different because the 3D thermal plume, after a certain time, become unstable and the whole field starts to oscillate as in the 2D situation. Fig. 10 shows that the 3D starting plume (at $t = 0.5$) across the cavity is very uniform in the central section $(2 < z < 8)$. Temperature contours at several z-planes are very similar in shape, penetration height and lateral extension, indicating that the 2D approximation can be invoked with prudence provided that the central cavity region is limited to $2 < z < 8$.

Between these bounds the averaged thermal plume flow field may be considered as weakly 3D in the Rayleigh and Prandtl

Table 3
Comparison of 2D versus 3D grids. The 3D aspect ratios are $\Gamma_{xy} = H/W = 5$, $\Gamma_{xz} = D/W = 10$. The Rayleigh and Prandtl numbers are $R = 10^5$ and $P = 0.71$ respectively. Nusselt numbers for the 3D grid were computed with eq. (4) and then averaged between $2 < z < 8$.

Grid size	$\langle Nu_l \rangle_x$	$\langle Nu_r \rangle_x$	$\langle \theta \rangle$
(41×201)	0.1694	0.1694	0.0396
$(41 \times 201 \times 401)$	0.1785	0.1785	0.0354

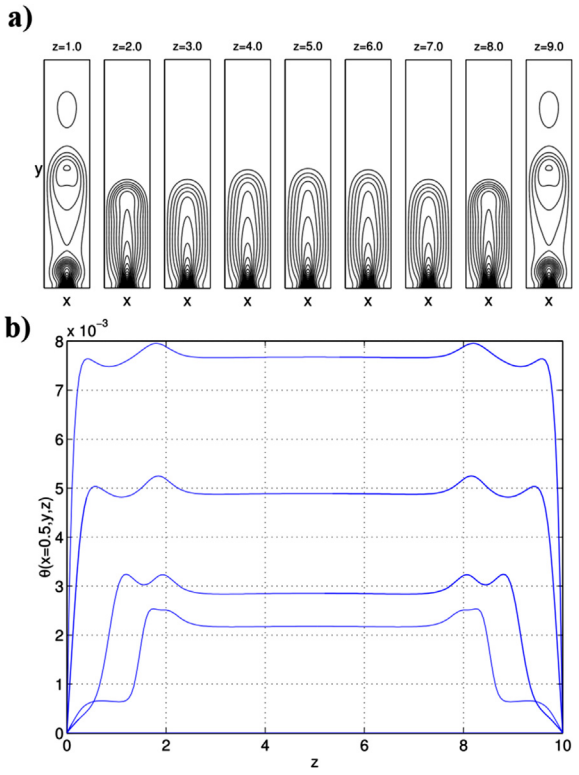

Fig. 10. 3D starting plume at $t = 0.5$. (a) Temperature contours for aspect ratios $\Gamma_{xy} = H/W = 5$, $\Gamma_{xz} = D/W = 10$ at $R = 10^5$ and $P = 0.71$. (b) Temperature profiles along the z-centerline at different heights $y = 0.1, 0.2, 0.5, 1.0$ at $R = 10^5$, $P = 0.71$.

number range here studied. After a given time ($t > 1$), temperature and velocity (not shown) snapshots of the starting thermal plume display sings of unsteadiness developing in phase along the z coordinate. Moreover, averaged Nusselt numbers have very similar values when compared to the 2D case (cf. Table 3).

In Figs. 11 and 12 we display a sequence of three dimensional temperature contours along the z coordinate at two time instants of the oscillating cycle for $R = 10^5$ and $P = 0.71$. We observe a weak dependence of the thermal field along the z coordinate but having the same spatial phase, i.e., there is no phase lag of the local temperature fluctuations along z. This is a lock-in effect in the z coordinate which explain the persistence of the single transverse oscillation mode observed.

However, the upward plume motion observed is not uniform in the z coordinate, showing signs of a slight modulation and 3D effects across the longitudinal cavity axis (z). This effect is not so

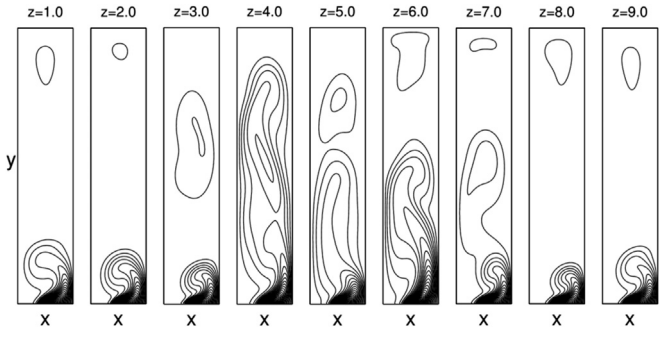

Fig. 11. 3D temperature contours at different z-planes, for aspect ratios $\Gamma_{xy} = H/W = 5$, $\Gamma_{xz} = D/W = 10$ at $R = 10^5$ and $P = 0.71$. Simulation time.$t = 1.7$.

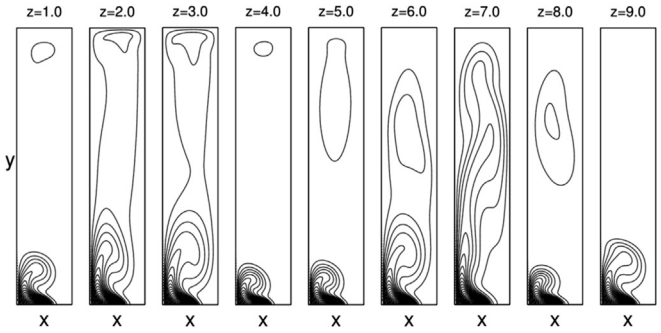

Fig. 12. 3D temperature contours at different z-planes, for aspect ratios $\Gamma_{xy} = H/W = 5$, $\Gamma_{xz} = D/W = 10$ at $R = 10^5$ and $P = 0.71$. Simulation time.$t = 2.7$.

strong to destroy the transverse oscillation, indicating that the influence of the slender cavity aspect ratio plays a dominant role on the lock-in oscillation of the plume. The z-gradients resulting from the front ($z = 0$) and back ($z = 10$) walls are unable to break the lock-in overall behavior but can make appear a longitudinal mode. We expect however, a break in the phase locked regime at higher R or higher Γ_{xz} aspect ratios.

5. Concluding remarks

Detailed numerical simulations of 2D thermal plumes inside a high aspect ratio cavity were performed using the SIMPLER method. Thermal plumes were produced by a discrete heater mounted flush with the bottom wall. Most of the simulations were done keeping a constant cavity aspect ratio $\Gamma_{xy} = 5$, in order to track the vertical motion of the thermal plume as a response to changes in both fluid Prandtl number and Rayleigh number. We found evidence of a flow transition from a steady state into a periodic oscillating pattern when we increased the Rayleigh and Prandtl numbers. The overall flow unsteadiness was associated with flow instabilities characterized by a periodic but upward propagative motion of the thermal plume cap in both transverse and vertical directions. A possible mechanism of flow instability, in such a slender cavity, could be attributed in part to shear stresses between ascending and descending fluid layers, like a Kelvin–Helmholtz instability. We have observed that instabilities of the plume may arise at two very different Prandtl numbers, where the frequency of the most unstable mode is an increasing function of the Rayleigh number R. However, when we keep R constant, the observed frequency of this mode decreases with Prandtl number, probably because an increase in momentum diffusivity will raise the viscous damping of flow fluctuations. The system appears here looking for a more efficient way of energy dissipation through the onset of instabilities giving rise to a complex fluid and thermal pattern inside the box. It seems that there exists a threshold for the Rayleigh number, R_c, which would explain the transition from a steady to an unstable thermal plume. This value depends on the fluid properties as it was found to decrease if we decrease the Prandtl number. It has been found that at constant Rayleigh and Prandtl numbers, higher aspect ratio of the cavity will favor the flow unsteadiness and therefore the onset of the flow instability. Finally, in order to check the validity and limits of the 2D approximation, we performed numerical simulation checks on a three dimensional box of same cross section dimensions under the same boundary conditions. These results confirmed the onset of unsteadiness of the plume produced by similar transverse oscillations predicted by the 2D numerical simulation. The 3D checks confirmed that the plume oscillates in phase across the z-

coordinate, under a locked transverse oscillation mode but also showing signs of a modulation and 3D effects across the cavity *z*-axis.

References

[1] J.S. Turner, Buoyancy Effects in Fluids, Cambridge University Press, 1973.
[2] E. Moses, G. Zocchi, I. Procaccia, A. Libchaber, The dynamics and interaction of laminar thermal plumes, Europhys. Lett. 14 (1991) 55–60.
[3] I. Sezai, A.A. Mohamad, Natural convection from a discrete heat source on the bottom of a horizontal enclosure, Int. J. Heat. Mass Transf. 43 (2000) 2257–2266.
[4] L. van Haren, F.T.M. Nieuwstadt, A large-eddy simulation of buoyant plumes in a convective boundary layer, Il Nuovo Cimento 13C (6) (1990) 923–931.
[5] R. Hernández, A. Campo, Pattern formation in thermal plumes, EUROTHERM-36, in: Advanced Concepts and Techniques in Thermal Modelling, 1994, pp. A56–A62. Poitiers (France).
[6] D.J. Shlien, L. Boxman, Laminar starting plume temperature field measurement, Int. J. Heat. Mass Transf. 24 (5) (1981) 919–931.
[7] L. Pera, B. Gebhart, On the stability of laminar plumes: some numerical solutions and experiments, Int. J. Heat. Mass Transf. 14 (1971) 975–984.
[8] J.C. Elicer-Cortés, C. Ruz, R.H. Hernández, M. Pavageau, D. Boyer, Observation of preferred instability modes in a mechanically excited thermal plume using schlieren visualizations, Int. Comm. Heat Mass Transf. 32 (2005) 360–370.
[9] J.C. Elicer-Cortés, C. Baudet, Ultrasound scattering from a turbulent round thermal pure plume, Exp. Therm. Fluid Sci. 18 (1999) 271–281.
[10] T. Cortese, S. Balachandar, Vortical nature of thermal plumes in turbulent convection, Phys. Fluids 5 (12) (1993) 3226–3232.
[11] M.L. Chadwick, B.H. Webb, H.S. Heaton, Natural convection from two-dimensional discrete heat sources in a rectangular enclosure, Int. J. Heat. Mass Transf. 34 (7) (1991) 1679–1693.
[12] S. Banerjee, A. Mukhopadhyay, S. Sen, R. Ganguly, Natural convection in a bi-heater configuration of passive electronic cooling, Int. J. Therm. Sci. 47 (2008) 1516–1527.
[13] S.V. Patankar, Numerical Heat Transfer and Fluid Flow, Hemisphere Publishing Corporation, Washington D.C., 1980.
[14] R. Hernández, R.L. Frederick, Spatial and thermal features of three dimensional Rayleigh Bénard convection, Int. J. Heat. Mass Transf. 37 (3) (1994) 411–424.
[15] R. Hernández, Influence of the heating rate on supercritical Rayleigh–Bénard convection, Int. J. Heat. Mass Transf. 38 (16) (1995) 3035–3051.
[16] O. Turan, A. Sachdeva, R.J. Poole, N. Chakraborty, Laminar natural convection of power-law fluids in a square enclosure with differentially heated sidewalls subjected to constant wall heat flux, J. Heat Transf. 134 (12) (2012) 122504.1–122504.15.
[17] G. de Vahl Davis, Natural convection of air in a square cavity: a bench mark numerical solution, Int. J. Numer. Methods. Fluids 3 (1983) 249–264.
[18] P.G. Drazin, W.H. Reid, Hydrodynamic Stability, Cambridge University Press, 1981.